

Influence of Non-Uniform Distribution of Acoustic Wavefield Strength on Time-Distance Helioseismology Measurements

Konstantin V. Parchevsky, Junwei Zhao, and Alexander G. Kosovichev

*W. W. Hansen Experimental Physics Laboratory, Stanford University, Stanford, CA
94305-4085*

kparchevsky@solar.stanford.edu

ABSTRACT

By analyzing numerically simulated solar oscillation data, we study the influence of non-uniform distribution of acoustic wave amplitude, acoustic source strength, and perturbations of the sound speed on the shifts of acoustic travel times measured by the time-distance helioseismology method. It is found that for short distances, the contribution to the mean travel time shift caused by non-uniform distribution of acoustic sources in sunspots may be comparable to (but smaller than) the contribution from the sound speed perturbation in sunspots, and that it has the opposite sign to the sound-speed effect. This effect may cause some underestimation of the negative sound-speed perturbations in sunspots just below the surface, that was found in previous time-distance helioseismology inferences. This effect cannot be corrected by artificially increasing the amplitude of oscillations in sunspots. For large time-distance annuli, the non-uniform distribution of wavefields does not have significant effects on the mean travel times, and thus the sound-speed inversion results. The measured travel time differences, which are used to determine the mass flows beneath sunspots, can also be systematically shifted by this effect, but only in an insignificant magnitude.

Subject headings: Sun: helioseismology – Sun: oscillations – sunspot

1. Introduction

Time-distance helioseismology is based on measuring and inverting acoustic wave travel times between separate points on the surface of the Sun. It is one of widely used approaches of local helioseismology for reconstructing solar subsurface structures and flows. Calculation of the temporal cross-covariance of two oscillation signals, observed in different points on

the solar surface, is a key element of this method (Duvall et al. 1993). Kosovichev & Duvall (1997) showed that the cross-covariance function for waves with the phase speed lying in a narrow interval can be approximately represented by a Gabor wavelet. The phase and group travel times of acoustic waves can be obtained by fitting the Gabor wavelet to the observed cross-covariance function, using a least-square method. The measured phase travel times are used for inferring the subphotospheric perturbations of the sound (wave) speed and flow velocities in the quiet Sun and sunspot regions (Kosovichev et al. 2000; Zhao et al. 2001). The mean travel time of acoustic waves traveling between two points in the opposite directions are used for determining the sound speed, and the travel time difference is used for determining the flows.

However, an accurate inference of sunspot’s subsurface sound-speed structures and flow fields by use of this approach may be affected by a series of physical and unphysical effects, such as strong wave damping in active regions (Woodard 1997), and the presence of strong magnetic field (Zhao & Kosovichev 2006). Recently, by using observations of a quiet Sun region and artificially reducing solar acoustic oscillation amplitudes, i.e. masking solar wavefield to mimic the sunspot’s behavior, Rajaguru et al. (2006) found that this procedure could shift the measured acoustic travel times systematically by an amount of 5 – 40%, although such a shift was not expected. Furthermore, they suggested to correct the observed acoustic wavefields inside active regions by artificially increasing the wave amplitude.

However, it is evident that the artificially masked wavefield of a solar quiet region can only mimic the acoustic power of the active region, but not the actual physical cause. Therefore, the systematic errors estimated by this approach may be inaccurate, and the correction procedure is unjustified. In this paper, we have carried out 3D numerical simulations of solar oscillations based on three different models to mimic the sunspot’s wavefield, and investigated the systematic errors caused by the amplitude effects in the time-distance measurements. These models include the artificial masking the numerically simulated wavefields, as suggested by Rajaguru et al. (2006), reducing the strength of oscillation sources to reflect the physical effect of reduced excitation in sunspots (Parchevsky & Kosovichev 2007a), and compare these with effects caused by using a sound-speed perturbation deduced by the previous sound-speed inversions (Kosovichev et al. 2000). The numerical simulation procedure and results are described in §2, and the results of the time-distance analysis are given in §3, followed by discussions in §4.

2. Numerical Simulations

2.1. Governing Equations

Propagation of acoustic waves on the Sun is described by the system of the linearized Euler equations

$$\begin{aligned} \frac{\partial \rho'}{\partial t} + \nabla \cdot (\rho_0 \mathbf{u}') &= 0 \\ \frac{\partial}{\partial t}(\rho_0 \mathbf{u}') + \nabla p' &= \mathbf{g}_0 \rho' + \mathbf{f}(x, y, z, t), \end{aligned} \tag{1}$$

where \mathbf{u}' is the velocity perturbation, ρ' and p' are the density and pressure perturbations respectively, and $\mathbf{f}(x, y, z, t)$ is the function describing the acoustic sources. The pressure p_0 , density ρ_0 , and gravitational accelerations \mathbf{g}_0 with subscripts 0 correspond to the background model. To close the system (1) we used the adiabatic relation $\delta p/p_0 = \Gamma_1 \delta \rho/\rho_0$ between Lagrangian variations of pressure δp and density $\delta \rho$. The adiabatic exponent Γ_1 is calculated from the realistic OPAL equation of state (Rogers et al. 1996) for the hydrogen X and heavy elements Z abundances of the standard model. The standard solar model S (Christensen-Dalsgaard et al. 1996) with a smoothly joined model of the chromosphere of Vernazza et al. (1976) is used as the background model.

The standard solar model is convectively unstable, especially in the superadiabatic sub-photospheric layers where convective motions are very intense and turbulent. Using this convectively unstable model as a background model leads to the instability of the solution of the linear system. The condition for stability against convection requires that the square of Brunt-Väisälä frequency $\mathcal{N}_0^2 = g_0(1/\Gamma_1 \text{d log } p_0/\text{d}r - \text{d log } \rho_0/\text{d}r)$ is positive. To make the background model convectively stable we replaced all negative values of \mathcal{N}_0^2 by zeros and recalculated the profiles of pressure and density from the condition of hydrostatic equilibrium. This procedure guarantees convective stability of the background model. It has been shown that the profiles of pressure p_0 , density ρ_0 , sound speed c_0 , and acoustic cut-off frequency $\omega_c^2 = c_0^2/4H_\rho^2(1 - 2 \text{d}H_\rho/\text{d}r)$ of the modified model are very close to the corresponding profiles of the standard solar model (Parchevsky & Kosovichev 2007b). Quantity $H_\rho^{-1} = -\text{d log } \rho_0/\text{d}r$ represents the density height scale.

To prevent spurious reflections of acoustic waves from the boundaries we established non-reflecting boundary conditions based on the Perfectly Matched Layer (PML) method (Hu 1996) at the top and bottom boundaries. The top boundary was set at the height of 500 km above the photosphere. This simulates a realistic situation when not all waves are reflected from the photosphere. Waves with frequencies higher than the acoustic cut-off frequency pass through the photosphere and are absorbed by the top boundary. This naturally introduces frequency dependence of the reflecting coefficient of the top boundary.

The lateral boundary conditions are periodic. The details are described by Parchevsky & Kosovichev (2007b).

The waves are generated by spatially localized sources of the z-component of force

$$\mathbf{f}(x, y, z, t) = \begin{cases} \mathbf{e}_z A \left[1 - \left(\frac{r}{R_{src}} \right)^2 \right]^2 (1 - 2\tau^2) e^{-\tau^2} & \text{if } r \leq R_{src} \\ 0 & \text{if } r > R_{src} \end{cases} \quad (2)$$

with r and τ given by

$$r = \sqrt{(x - x_{src})^2 + (y - y_{src})^2 + (z - z_{src})^2}, \quad \tau = \frac{\omega(t - t_0)}{2} - \pi, \quad t_0 \leq t \leq t_0 + \frac{4\pi}{\omega} \quad (3)$$

where \mathbf{e}_z is the unit vector in the vertical direction, x_{src} , y_{src} , and z_{src} are the coordinates of the center of the source, R_{src} is the source radius, ω is the central frequency, t_0 is the moment of the source ignition, A is the coefficient, which is measured in dyn cm^{-3} and describes the source strength. It has a physical meaning of the force density.

2.2. Numerical Method

To solve the system (1), a semi-discrete code developed by Parchevsky & Kosovichev (2007b) is used. The high-order dispersion relation preserving (DRP) finite difference (FD) scheme of Tam & Webb (1993) is used for spatial discretization. The coefficients of this FD scheme are chosen from the requirement that the error in the Fourier transform of the spatial derivative is minimal. It can be shown that the 4th-order DRP FD scheme describes short waves more accurately than the classic 6th-order FD scheme. A 3rd-order, three-stage strong stability preserving Runge-Kutta scheme with the Courant number, $C = 1$, (Shu 2002) is used as a time advancing scheme.

The efficiency of the high-order FD schemes can be reached only if they are combined with adequate numerical boundary conditions. We followed Carpenter et al. (1993) and used an implicit Padé approximation of the spatial derivatives near the top and bottom boundaries to derive a stable 3rd-order numerical boundary conditions consistent with the 4th-order DRP numerical scheme for interior points of the computational domain.

Waves with the wavelength less than $4\Delta x$ are not resolved by the FD scheme. They lead to point-to-point oscillations of the solution that can cause a numerical instability. Such waves have to be filtered out, and we use a 6th-order digital filter to eliminate unresolved short wave component from the solution at each time step.

2.3. Simulation of Artificial Data

The simulations are carried out in a rectangular domain of size $90 \times 90 \times 31$ Mm³ using a uniform $600 \times 600 \times 619$ grid. The background model varies sharply in the region above the temperature minimum. Thus, to simulate the propagation of acoustic waves into the chromosphere we choose the vertical spatial step $\Delta z = 50$ km in order to preserve the accuracy and numerical stability. The spatial intervals in the horizontal direction are $\Delta x = \Delta y = 150$ km. To satisfy the Courant stability condition for the explicit scheme, the time step is set to be equal to 0.5 seconds. The sources of the z-component of force with random amplitudes and uniform frequency distribution in the range of 2 – 8 mHz are randomly distributed at the depth of 100 km below the photosphere and are independently excited at arbitrary moments of time.

We describe three sets of simulations with different distribution of acoustic sources and different background models. The first reference model (Model I) represents simulations of the acoustic wave field for horizontally uniform distribution of the acoustic sources and the horizontally uniform background model. This model corresponds to the quiet Sun and will be used as a reference state for the following time-distance analysis. The acoustic travel times for models II and III are computed relatively to this reference model. The goal of this study is to estimate the contributions to the travel times arising from perturbations of the background model and non-uniform distribution of the acoustic sources separately. For this purpose, in model II the acoustic source strength is gradually decreased (masked) in the central region, simulating the reduction of the acoustic sources in sunspots (Parchevsky & Kosovichev 2007a). In this model, the horizontal axially symmetric distribution of the acoustic source strength is given by formula

$$A(x, y) = \begin{cases} \frac{1}{2} \left(1 - \cos \frac{\pi r_h}{R_s} \right) & \text{if } r_h \leq R_s \\ 1 & \text{if } r_h > R_s, \end{cases} \quad (4)$$

where $r_h = \sqrt{(x - x_s)^2 + (y - y_s)^2}$ is the horizontal distance from the sunspot axis, x_s , y_s , and R_s are the x-, y- coordinates of the sunspot center and the sunspot radius respectively. The background model remains unperturbed and horizontally uniform. So, as far as the background model remains unchanged all deviations of simulated wave field properties from model I can be explained as a result on non-uniform distribution of the acoustic sources.

Strictly speaking, travel times for the cases of uniform distribution of the acoustic sources (Model I) and masked source strength (Model II) are calculated at different conditions. The amplitude of the wave field is uniform in the first case and non-uniform in the second one. To take this into account we mask the *wave field* of the Model I by masking function computed by

averaging signals azimuthally around the sunspot center. This mimics the reduced amplitude of active regions, just as what was done by Rajaguru et al. (2006). The resultant model is called Model Ia for the convenience of reference in the following descriptions. Although the amplitude distributions now are the same for both wave fields, the wave fields itself are different, because masking of the source strength is not reduced to simple masking of the resulting wave field.

Model III combines the source masking of Model II with the sound speed perturbation in sunspots. The 3D sound-speed profile c in Model III is approximated by the formula

$$c(x, y, z) = c_0(z) \left[1 + \frac{\delta c(z)}{c_0(z)} (1 - A(x, y)) \right], \quad (5)$$

where $\delta c/c_0$ is the vertical profile of the sound speed perturbation at the sunspot axis. This profile is shown in Figure 1 and was calculated from the inversion of helioseismic data for the sunspot observed by SOHO/MDI on 20 June 1998 (Kosovichev et al. 2000). The change of the sound-speed perturbation sign from negative to positive at approximately 4 Mm below the photosphere is a characteristic feature of this profile. The depth of inversion divides the domain in vertical direction into two regions with the sound speed greater and smaller than in the standard reference model. Hence, we expect different behavior of waves propagating through this artificial sunspot if their turning points lie in different regions.

The amplitude map of the resulting wave field for Model III is shown in the left panel of Figure 2. The solid line in the right panel represents the azimuthally averaged amplitude profile. The dashed line shows the angularly averaged amplitude profile for Model II. The inhomogeneity of the sound speed causes increasing the ratio of oscillation amplitudes outside and inside of the artificial sunspot by about 40%.

The acoustic power spectrum (k - ω diagram) of the simulated wave field is shown in Figure 3. We see a good agreement with the observed power spectrum in terms of the shape and locations of power ridges, yet the simulated wave field has more power in high-frequency region. It is not clear whether such power excess really exists and instrumentally filtered out during observations or it is an artifact of the numerical modeling of the wave field. The realistic non-linear simulations of solar convection also show a power excess in the k - ω diagram at higher frequencies (Georgobiani et al. 2007). For the present study, the high-frequency power excess is unimportant, because for the time-distance helioseismology analysis, we only select the frequency band of 3 – 4 mHz for analysis, and in this range, the simulated acoustic power is similar to the observations.

3. Results

3.1. Time-Distance Analysis

To perform the time-distance helioseismology analysis of the simulated data we followed the procedure described in Zhao et al. (2001). For all our models, we select the annuli with radii of 6.2 – 11.2 Mm, 8.7 – 14.5 Mm, and 14.5 – 19.4 Mm to obtain the mean travel times, $\tau_{\text{mean}}^{(i)}$, and the travel time differences, $\tau_{\text{diff}}^{(i)}$, (index i marks model number, including the reference Model I), which are respectively averages and differences of outgoing and ingoing travel times in the time-distance center-annulus measurement scheme. A phase-speed filter is applied in each case to select only waves in a narrow phase speed interval. To study the effects caused by wavefield non-uniformity, we calculate the differences of $\delta\tau_{\text{mean}}^{(i)} = \tau_{\text{mean}}^{(i)} - \tau_{\text{mean}}^{(\text{I})}$ and $\delta\tau_{\text{diff}}^{(i)} = \tau_{\text{diff}}^{(i)} - \tau_{\text{diff}}^{(\text{I})}$ for the analysis.

In Figure 4, we show the maps of the mean travel time perturbations, $\delta\tau_{\text{mean}}^{(i)}$, the travel time differences, $\delta\tau_{\text{diff}}^{(i)}$, for all three models. Although the background model of Models Ia and II are the same with the reference Model I, we can see systematic shifts of mean travel times inside the masked regions.

For better understanding the results, it is useful to compare the profiles of the travel time deviations, azimuthally averaged around the sunspot center for both $\delta\tau_{\text{mean}}^{(i)}$ and $\delta\tau_{\text{diff}}^{(i)}$, as shown in the middle row of Figure 5. Obviously, the mean travel time shifts, $\delta\tau_{\text{mean}}$, are significantly larger in Model II than in Model Ia, although both have exactly the same background model and exactly the same oscillation amplitude reduction in wavefields. Expectedly, Model III shows mostly positive travel time shifts in contrast with the other two models, and this is obviously due to the negative sound-speed perturbation to the background model in a shallow subsurface region. One would expect this positive time shift would increase significantly if there is no such effect that causes the time deficit in Model II, however, it is not immediately clear whether this is the case, or if it is, how much it would increase. For the travel-time difference, $\delta\tau_{\text{diff}}$, the shifts for all three models are quite small, within an order of 2 sec, substantially smaller than the measured travel time shifts from a real sunspot data (Zhao et al. 2001).

The azimuthally averaged $\delta\tau_{\text{mean}}^{(i)}$ and $\delta\tau_{\text{diff}}^{(i)}$ for the other two annuli measurements are also presented in Figure 5. For the shorter travel distances, both Models Ia and II show stronger travel time deficits in the mean travel time measurements compared the the intermediate travel distance case, up to approximately 15 sec for Model II. However, Model III still displays mostly a positive sign, although it displays some dips in the central area where one would expect a stronger positive shift because of the larger negative sound-speed perturbation there. Again, $\delta\tau_{\text{diff}}^{(i)}$ does not show any significant time shifts for all models. For the

larger annulus radius, Models Ia and II do not display significant time shifts, but Model III displays a significant negative time shift because for this set of measurement, waves reach the depth of a large positive sound-speed perturbation. For this annulus measurement, Models II and III display an order of magnitude of 5 sec travel time shifts in $\delta\tau_{\text{diff}}$, larger than those of shorter annuli measurements, but still significantly smaller than the shifts in the real sunspot measurements.

3.2. Power Correction

Based on their artificial tests with the quiet Sun data, in order to remove the measured travel time shifts caused by the oscillation amplitude reductions, Rajaguru et al. (2006) have suggested to make corrections for these areas by enlarging the observed oscillation amplitude in active regions. This procedure is just reverse to the artificial masking. It obviously works if the power reduction is caused by artificial masking, like in Model Ia. However, it is useful to examine whether this works for the oscillation power reductions that are not caused by surface masking, but physical mechanisms, such as the reduction in the excitation power (like in Models II and III).

For each model (Ia, II, and III) we calculate the average amplitude profile and normalized the wavefield by using this profile (procedure of unmasking the wavefield), making the oscillation power nearly uniform over the whole box. The same time-distance analysis is performed like in §3.1, and azimuthally averaged curves are displayed in Figure 6. It can be clearly seen that, as expected, this power correction removes all travel time shifts in both $\delta\tau_{\text{mean}}$ and $\delta\tau_{\text{diff}}$ for all annuli measurements for Model Ia. For $\delta\tau_{\text{mean}}$, for the two shorter annuli measurements, the correction slightly lifts both Models II and III without changing signs of the profiles, and for the longest annulus, the correction does not change much the measurements. For $\delta\tau_{\text{diff}}$, the correction changes the profiles of Models II and III for all annuli, but still, the travel time shifts are within 5 sec or so.

4. Discussion and Conclusion

The explanation of the fact that the acoustic travel times depend on the non-uniformness of the wave field amplitude or non-uniform distribution of the source strength is related to the definition of travel times in helioseismology, which have to deal with the stochastic randomly excited oscillations, rather than isolated point sources. The travel time of a wave packet traveling between two points on the surface is defined not as a local physical quantity, which

can be explicitly computed from the background model, but rather in an “observational” way as a parameter which is obtained from fitting of cross-correlation of the oscillation signals by the Gabor wavelet. Thus, it is very important to investigate the effect of non-uniform distribution of acoustic sources, damping and other causes of the non-uniform wave field distribution on the Sun. We have presented the results for some of these effects by using numerical 3D simulations of acoustic wave propagation in various solar models.

We have found that the source masking for horizontally uniform background model (dashed curves) may cause a systematic negative shift of about 8–13 seconds in the mean travel times for short distances (annuli with radii smaller than 14.5 Mm). Such travel time shift may cause underestimation of the sound speed perturbation in the shallow (1–2 Mm deep) subsurface layers. For larger distances, the contribution to the mean travel time shift becomes negligible. On the contrary, the shift of the travel time differences (due to the non-uniform distribution of the acoustic sources) is negligible for short distances and has a value about -5 sec for the largest distance used in our experiments. This is much smaller than perturbations of the travel-time differences observed in real sunspots.

The results of our experiments are different from a similar work by Hanasoge et al. (2007), where authors report significant disbalance between ingoing and outgoing travel times (about -5 s for distance of 6.2 Mm and about -15 s for distance of 24.35 Mm), and suggested that at the large distances the false travel time difference signal caused by non-uniform distribution of sources may be misinterpreted as a result of subsurface flows. However, it is quite clear that, as shown in the first two annuli measurements of Figure 5, the oscillation power deficit due to the source masking may have greatly reduced the travel time shifts measured in Model III, which means that if doing inversions, the inverted sound-speed profile would be greatly underestimated. This suggests that the sound-speed profile under sunspots obtained by Kosovichev et al. (2000) got the correct sign but might be underestimated. For the flow fields, this masking effect might cause some systematic velocity errors, but only of a very small magnitude.

In addition, our experiments show that the amplitude reduction is caused by the weaker oscillation sources in sunspots cannot be corrected by a simple normalization procedure. This imposes us a difficult task on how to retrieve accurately the sound-speed profiles beneath sunspots, and improve the time-distance helioseismology inferences.

REFERENCES

Carpenter, M.H., Gottlieb, D., and Abarbanel, S. 1993, *J. Comput. Phys.* 108, 272.

- Christensen-Dalsgaard, J., Däppen, W., Ajukov, S. V., Anderson, E. R., et al. 1996, *Science*, 272, 1286.
- Duvall, T. L., Jr., Jefferies, S. M., Harvey, J. W., & Pomerantz, M. A. 1993, *Nature*, 362, 430.
- Georgobiani, D., Zhao, J., Kosovichev, A. G., Benson, D., Stein, R. F., & Nordlund, A. 2007, *ApJ*, 657, 1157.
- Hanasoge, S. M., Couvidat, S., & Rajaguru, S. P. 2007, *ApJ*, submitted
- Hu, F. Q. 1996, *J. Comput. Phys.*, 129, 201.
- Kosovichev, A. G. & Duvall, T. L., Jr. 1997 in *Proc. SCORE'96: Solar Convection and Oscillations and their Relationship*, eds. F. P. Pijpers, J. Christensen-Dalsgaard, and C. S. Rosenthal, Kluwer Academic Publishers, Dordrecht, Holland, 241.
- Kosovichev, A. G., Duvall, T. L. Jr., & Sherrer, P. H. 2000, *Solar Phys.* 192, 159.
- Parchevsky, K. V., & Kosovichev, A. G. 2007a, *ApJ*, 666, L53
- Parchevsky, K. V. & Kosovichev, A. G. 2007b, *ApJ*, 666, 547.
- Rajaguru, S. P., Birch, A. C., Duvall, T. L. Jr., Thompson, M. J., & Zhao, J. 2006, *ApJ*, 646, 543.
- Rogers, F. J., Swenson, F. J., & Iglesias, C. A. 1996, *ApJ*, 456, 902.
- Shu, C.-W. 2002, in *Collected Lectures on the Preservation of Stability under Discretization*, eds. D. Estep and S. Tavener, SIAM, 51.
- Tam, C. and Webb, J. 1993, *J. Comput. Phys.* 107, 262
- Vernazza, J. E., Avrett, E. H., and Loeser, R. 1976, *ApJS*, 30, 1.
- Woodard, M. F. 1997, *ApJ*, 485, 890
- Zhao, J., & Kosovichev, A. G. 2006, *ApJ*, 643, 1317
- Zhao, J., Kosovichev, A. G., & Duvall, T. L., Jr. 2001, *ApJ*, 557, 384.

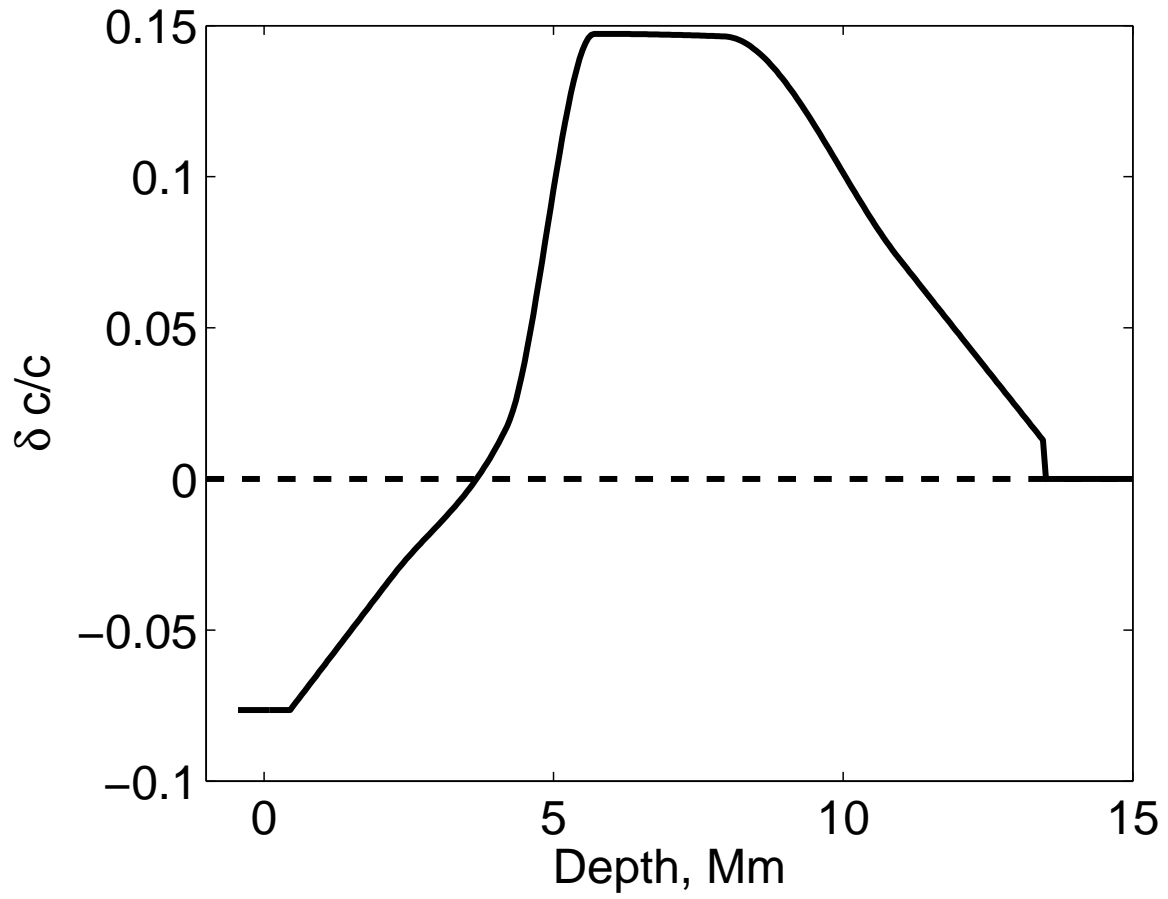


Fig. 1.— Perturbation of the sound speed profile at the sunspot axis, calculated by inverting data obtained from SOHO/MDI observations of the sunspot on 20 June 1998.

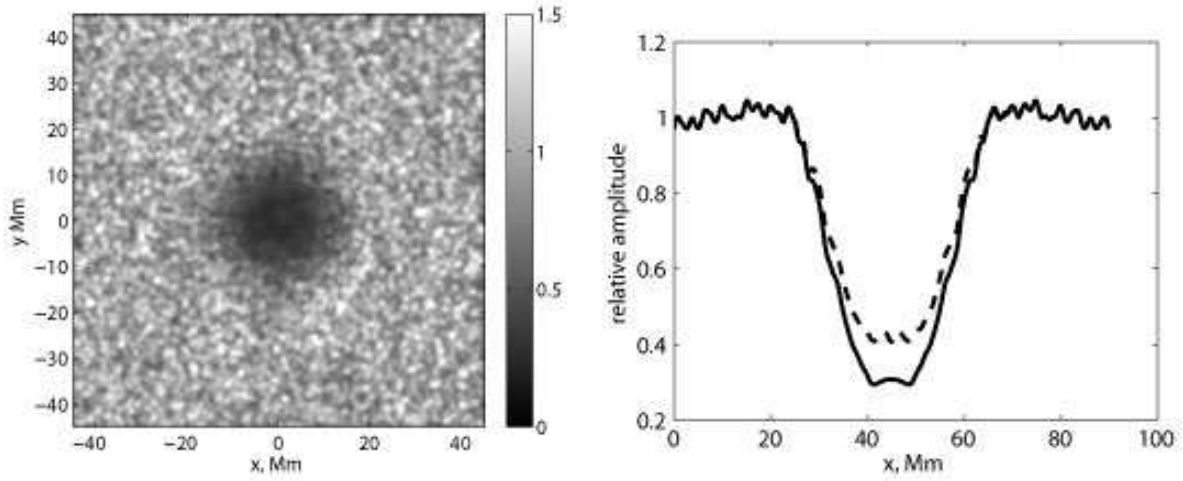


Fig. 2.— Amplitude map (*left*) of the vertical velocity component for simulations with masked sources and sound speed perturbation of the background model. The solid line represents azimuthally averaged profile of the map. The dashed line shows azimuthally averaged profile of the vertical velocity component for simulations with masked sources only (the background model is horizontally uniform).

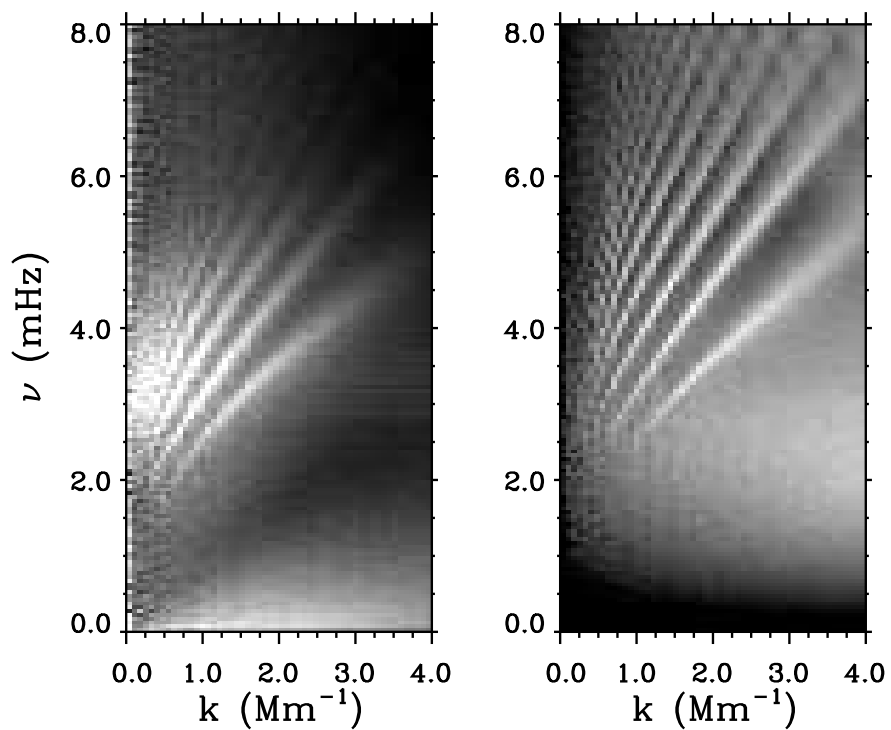


Fig. 3.— Power spectrum diagrams from MDI high resolution observations (*left*) and Model I of our simulations (*right*). Both power spectra are computed using the same time duration and after the simulated data are binned down to the same spatial resolution as the observed data.

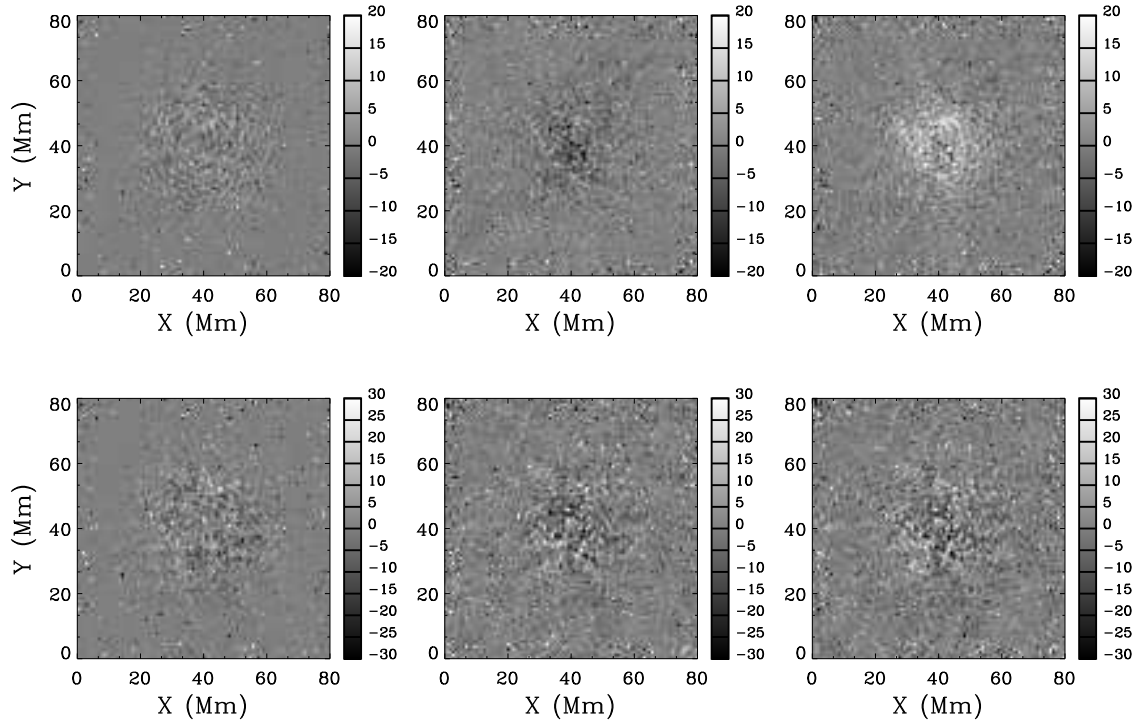


Fig. 4.— Maps for mean travel times (*upper row*) and travel time differences (*bottom row*) relative to the Model I. For both rows, from the left column to the right are for Model Ia, Model II, and Model III, respectively. Annulus radii used for time-distance measurements are from 8.7 to 14.5 Mm.

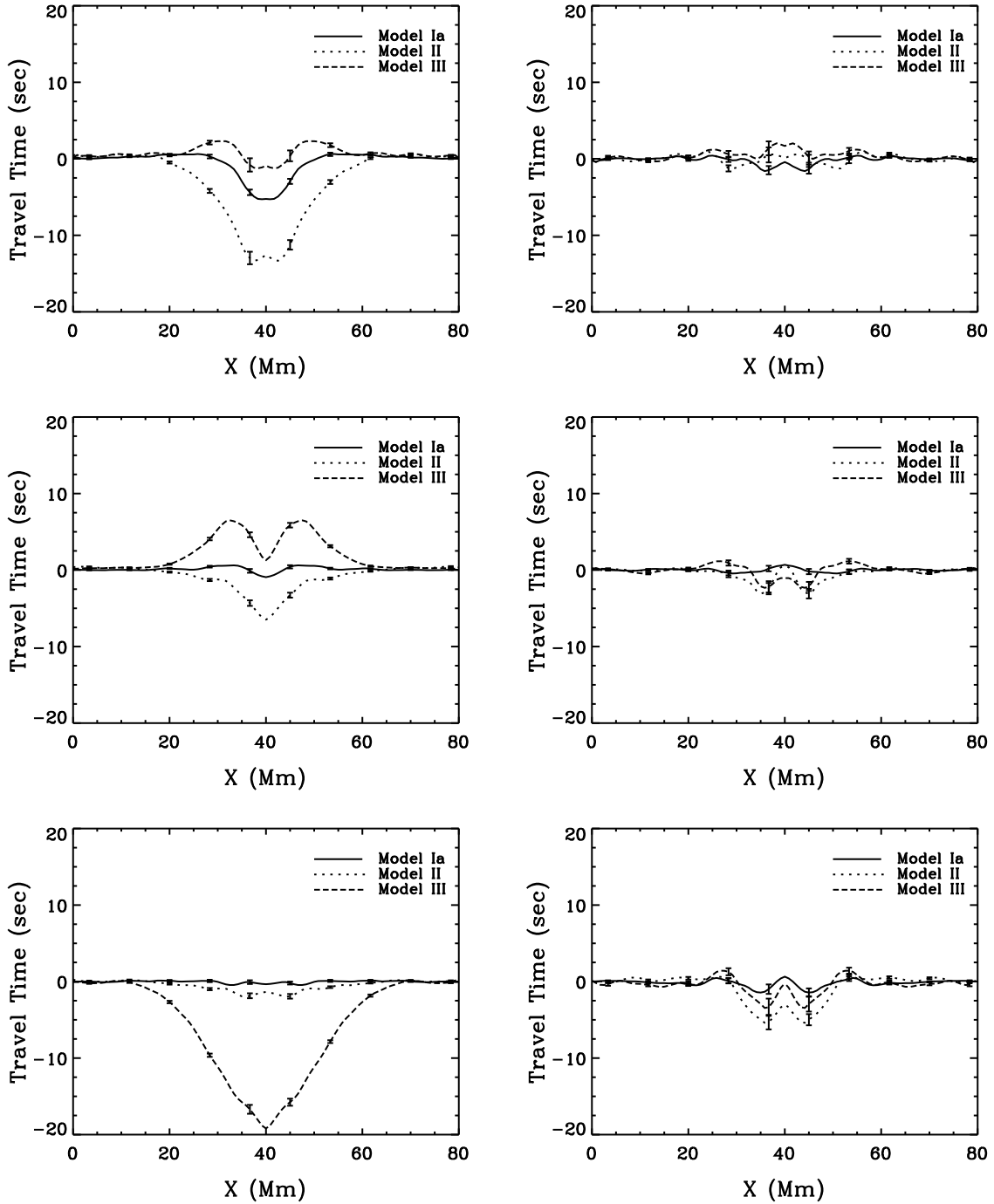


Fig. 5.— Mean travel times (*left panels*) and travel time differences (*right panels*) azimuthally averaged from maps like shown in Figure 4 for different annulus radii of (from above to bottom) 6.2 – 11.2 Mm, 8.7 – 14.5 Mm, and 14.5 – 19.4 Mm.

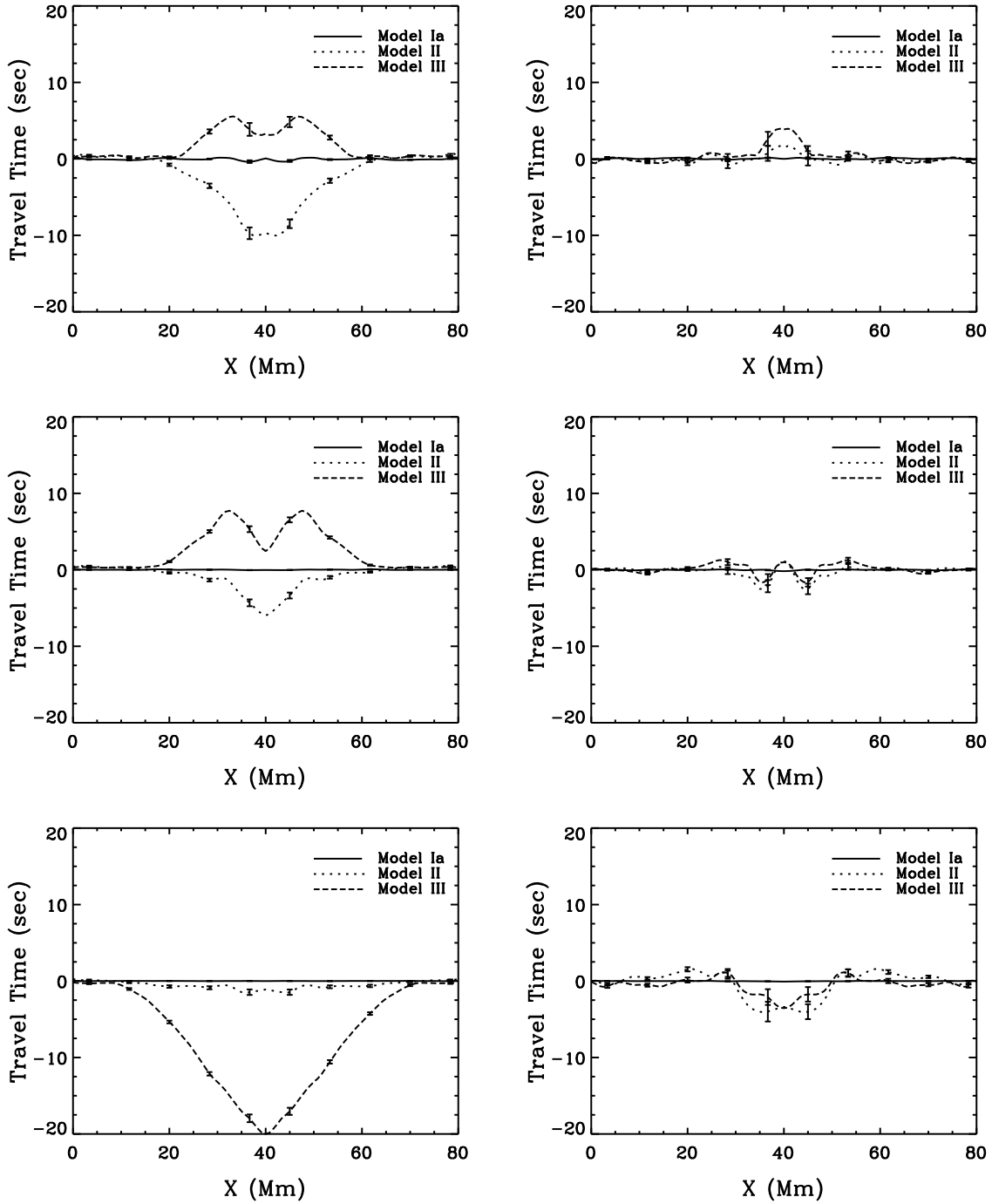


Fig. 6.— Same as Figure 5, but after the power corrections.